CHAPTER EIGHT

# Collision processes using effective potentials

**Alejandra M.P. Mendez***, **Darío M. Mitnik**, **Jorge E. Miraglia**
Instituto de Astronomía y Física del Espacio, Universidad de Buenos Aires – Consejo Nacional de Investigaciones Científicas y Técnicas, Buenos Aires, Argentina
*Corresponding author: e-mail address: alemendez@iafe.uba.ar

## Contents

## Abstract

We investigate the feasibility of using pseudopotentials to generate the bound and continuum orbitals needed in collisional calculations. By examination of several inelastic processes in the first Born approximation, we demonstrate the inconveniences of this approach. Instead, we advocate use of effective potentials obtained with the depurated inversion method (DIM). In this contribution, we extend this method to molecular systems. Calculations of single first-order photoionization and proton-impact ionization using the DIM show fair agreement with experimental results for both atoms and molecules.

*Advances in Quantum Chemistry*, Volume 79
ISSN 0065-3276
https://doi.org/10.1016/bs.aiq.2019.05.003

## 1. Outline

Inelastic transition calculations require the representation of the bound and continuum states involved in the collisional processes. The hypothetical existence of an effective one-electron local potential accounting for these states would allow more direct generation of the orthogonal wavefunctions for the interacting particles. This approach should include individual *nl*-orbital potentials, a feature missing from most of the standard density functional methods. The idea of replacing a many-body, nonlocal interaction by an effective one-electron equation opens up the possibility of studying extremely complex systems with high accuracy.

In this context, one promising idea emerges from the pseudopotential approximation (PPA), in which all the complexity of the wavefunctions near the core—that usually consumes a huge numerical effort—is avoided. For instance, density functional theory codes using pseudopotentials, such as the PARSEC, for example,[1,2] permit the use of an equally spaced grid involving a relatively small number of points. Otherwise, the use of realistic potentials describing the nucleus Coulomb potential requires a high density of points concentrated at the origin to describe what the pseudopotentials cast aside. Thus, if PPA was applicable in the field of collision theory, one would save an enormous amount of computational resources.

Another interesting approach is the depurated inversion method (DIM),[3–5] which allows accurate, effective potentials to be obtained by substituting the coupled multielectron equations into a Kohn–Sham-type equation. In the first step, the potential is obtained through inversion of the one-electron equation. Next, a careful optimization of the potential is carried out, eliminating poles, and imposing the appropriate boundary conditions analytically. In that way, the DIM potentials are parametrized in simple analytical expressions.

In the present work, we explore the possibility of implementing an effective potential approximation in the atomic collision theory to describe inelastic processes. In particular, we examine several collisional processes involving a single electron transition: photoionization, excitation, ionization, and electron capture. A wide variety of ab initio methods have been implemented to compute scattering cross sections for atomic targets, from the early implementations of the first Born approximation (FBA),[6,7] to more sophisticated fully quantum mechanical methods, e.g., Refs. 8–11. Whether for atoms or molecules, we shall present cross sections and compare with some experimental data. We do not wish, here, to present a detailed comparison with existing calculations. The main purpose is to illustrate the effective use of the DIM in collision applications. To this end, several simplifications are made (1) The calculations are constrained to Hamiltonians describing only the moving projectile, the target, and the active electron; (2) The transition-matrix elements are only considered in first perturbative order. If the first-order fails, it would not make any sense to extend the calculation to higher terms of the series. For simplicity, we will restrict our calculations only to the FBA framework, which is known to give reasonable agreement with the experimental cross section in the intermediate—high projectile energy range. Moreover, within this energy range and approximation order, the Hartree–Fock orbitals are known to provide the correct high energy limit.

We examine the above mentioned inelastic processes for two atoms with a single outer electron: hydrogen and lithium. In this context, we inspect the influence of the target description in the cross sections when the PPA and DIM approaches are implemented. Furthermore, these effects have been previously studied in other perturbative approaches, i.e., the continuum distorted wave eikonal-initial-state (CDW-EIS), for various targets (for example, see Refs. 12, 13). The DIM approach is further tested in the case of many-electron atoms by comparing photoionization cross sections with experimental measurements.

On the other hand, the description of molecular systems constitutes a real challenge due to their nonspherical symmetry and multicenter character. Many ab initio and semiempirical theoretical approximations[14–16] have been developed to this end over the last century. In this work, we present an extension of the DIM method for simple molecular systems, providing a new parametric expression for the potentials. The target description is once again tested by examination of its performance in first-order collisional processes, and the methane molecule being taken as an example.

## 2. Theory

### 2.1 Pseudopotential approximation

The pseudopotential approximation consists in replacing the Coulomb potential in the many-electron system Hamiltonian with a smooth function so that the electron wavefunctions oscillating rapidly in the core region are replaced by nodeless pseudo-orbitals having the right energy and the same outer range properties. In general, the pseudopotentials $V_{\mathrm{PP}}$ can be defined through a pseudocharge $Z_{\mathrm{PP}}$ as

$$V_{\mathrm{PP}}(r) = -\frac{Z_{\mathrm{PP}}(r)}{r}, \tag{1}$$

$$Z_{\mathrm{PP}}(r) = \begin{cases} f(r), & r \leq r_c \\ 1, & r > r_c \end{cases}, \tag{2}$$

where $r_c$ is a cutoff radius that separates the core, $r \leq r_c$, from the valence region, $r > r_c$, of the target and $f(r)$ is a continuous function with a constant value at the origin. Fig. 1 illustrates a pseudopotential (solid line) and its corresponding pseudo-wavefunction for the 3*s* orbital of argon. Notice that the pseudopotential behaves as $-r^{-1}$ (dot-dash line) in the valence region, as defined in Eqs. (1) and (2). The pseudo-wavefunction agrees with the one-electron Hartree–Fock (HF) orbital (dashed line) in the outer region, losing all information about the atomic structure close to the origin.

In Section 3, we analyse the feasibility of implementing pseudopotentials in collisional processes calculations for two simple atomic targets: hydrogen and lithium. For each atom, the following pseudopotentials are examined

| Name | Source | Type | Refs. |
|---|---|---|---|
| $A$ | ABINIT | GGA | 17, 18 |
| $P$ | PARSEC | Troullier Martins | 1, 2 |

(3)

The hydrogen atom has only one electron, and the corresponding pseudopotential is not essential. However, the hydrogen pseudopotentials from (3) reproduce with high accuracy the main features of the wavefunctions, even for excited states.

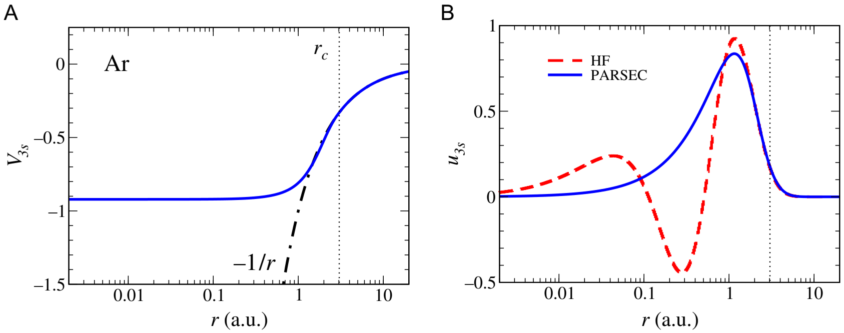

**Fig. 1** (A) Pseudopotential, (B) pseudo-wavefunction and HF orbital for the 3*s* orbital of argon.

We will now proceed to examine the pseudocharges and its one-electron solutions for the lithium atom closely. First, we study the spatial and momentum representation of the pseudocharges. The momentum-space equivalent of $Z(r)$ is given by the Fourier transform

$$\tilde{Z}(k) = \frac{1}{\sqrt{2\pi}} \int_{-\infty}^{+\infty} Z(r)\, e^{-ikr}\, dr. \tag{4}$$

The pseudocharges from (3) for the 2*s* orbital of lithium are illustrated in Fig. 2. For comparison, we include the potential obtained from implementing the depurated inversion method described in Section 2.2. The pseudocharges vanish at the origin, avoiding the divergence of the Coulomb potential. However, this feature comes at a price: the pseudocharges in the spatial representation are repulsive around $r = 1$ a.u., and their momentum picture fails to represent the target for high $k$, showing an incorrect oscillatory behavior for values greater than $k_c = (2\pi r_c)^{-1} \sim 0.7$ a.u..

Secondly, we inspect the behavior of the bound pseudo-orbitals obtained from solving the one-electron Schrödinger equation with a pseudopotential. As usual, the bound state wavefunctions can be written as

$$\psi_{nlm}(\mathbf{r}) = \frac{u_{nl}(r)}{r} Y_l^m(\hat{r}), \tag{5}$$

where $u_{nl}(r)$ are the reduced radial wavefunctions, and $Y_l^m(\hat{r})$ are the spherical harmonics. Similarly, the Fourier transform of these functions is given by

$$\tilde{\psi}_{nlm}(\mathbf{k}) = \frac{\chi_{nl}(k)}{k} Y_l^m(\hat{k}). \tag{6}$$

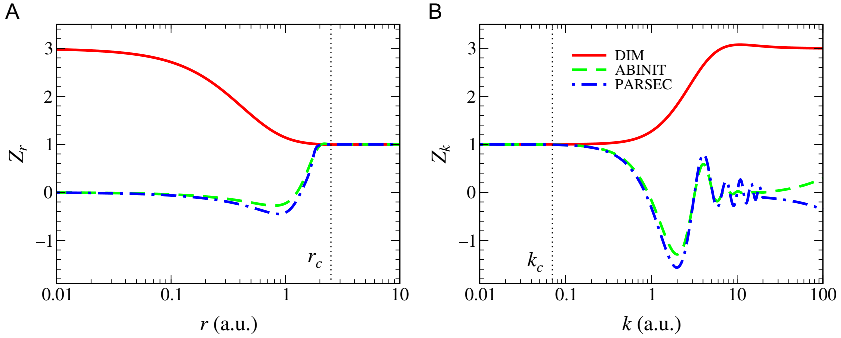

**Fig. 2** Pseudo and DIM charges for the 2*s* orbital of lithium. (A) Spatial and (B) momentum representation.

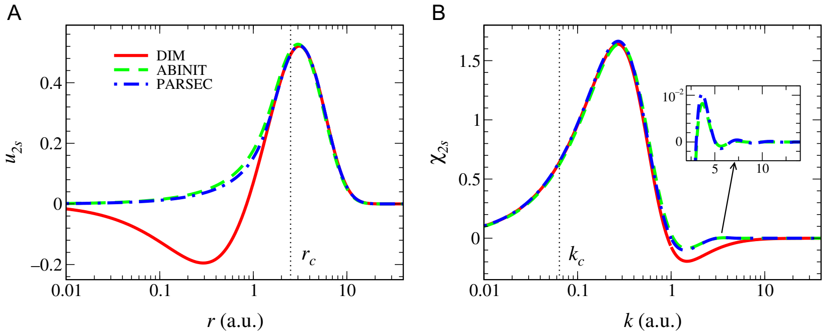

**Fig. 3** Pseudo and DIM bound state wavefunction for the 2*s* orbital of lithium in (A) spatial and (B) momentum representation.

The spatial and momentum representations of the 2*s* radial pseudo-wavefunctions of lithium corresponding to the pseudocharges from (3) are displayed in Fig. 3. Although the pseudo-orbitals are very different from the DIM 2*s* wavefunction, the transformed $\chi(k)$ seems to have similar characteristics. However, a closer inspection of the tail region of these functions (see the inset of the figure) shows the existence of several nodes. We will see later that these discrepancies have significant consequences in the cross sections for most of the collisional processes examined.

Finally, the pseudopotential approach not only affects the representation of the bound orbitals but also determines the form of the continuum wavefunctions. For large *r*, the free state orbitals of an electron in the presence of a Coulomb potential can be written as

$$u_{kl}(r) \longrightarrow \sin\left(kr - l\frac{\pi}{2} - \eta \ln 2kr + \sigma_l + \delta_l\right), \tag{7}$$

where $k$ is the particle wave number, $\eta$ is Sommerfeld's parameter, $\sigma_l$ is the Coulomb phase shift, and $\delta_l$ is the wave phase shift with respect to the Coulomb wave.

Comparisons between the DIM (solid line) and the pseudo (dashed) continuum *ks* wavefunctions for lithium are shown in Fig. 4, close to the origin (left) and asymptotically (right). The pseudo and DIM wavefunctions behave similarly away from the nucleus. The asymptotic phase shift Δ accounts for the differences between the potentials. As the energy of the free electron increases, Δ diminishes. However, the orbitals in the core region are different even with increasing energy; the first maximum of the DIM wavefunctions is consistently smaller than of the pseudo-orbitals, which is understood since the Coulomb-type attraction of the nuclei is stronger than the pseudopotential in that region.

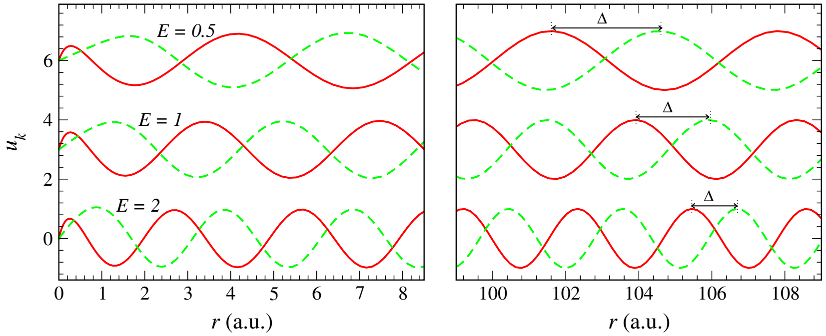

**Fig. 4** Continuum *ks* wavefunctions with energies *E* near the origin (*left*) and in the asymptotic region (*right*), calculated with the DIM potential (*solid line*) and the ABINIT pseudopotential (*dashed line*).

## 2.2 Depurated inversion method potentials

The depurated inversion method[3–5] consists of assuming that the many-electron atom orbitals can be represented by the solution of Kohn–Sham-type equations, in which the *nl* effective potentials are given by

$$V_{nl}(r) = \frac{1}{2}\frac{1}{u_{nl}(r)}\frac{d^2 u_{nl}(r)}{dr^2} - \frac{l(l+1)}{2r^2} + \varepsilon_{nl}, \tag{8}$$

where $u_{nl}$ and $\varepsilon_{nl}$ are the *nl* orbital wavefunctions and energies, respectively. In this work, the atomic structure is approximated with the Hartree–Fock method, which is computed with the HF codes by C. Froese Fischer[19] and the NRHF code by Johnson.[20] The computation of Eq. (8) poses various numerical problems. The nodes and asymptotic decay of the wavefunctions $u_{nl}(r)$ introduce significant numerical errors in the inversion procedure (see Ref. 5 for further details). The nodes of the orbitals produce huge unphysical poles, while the rapid asymptotic decay of the internal wavefunctions generates large divergences in the tail region of the potentials. The depuration method is implemented to tackle these unphysical features. An effective potential with a Coulomb-type shape $V_r(r) = -Z_r(r)/r$ is defined, and we enforce the correct boundary conditions fitting the inverted potential with the following analytical expression

$$Z_r(r) = \sum_{j=1}^{n} z_j e^{-\alpha_j r}(1 + \beta_j r) + 1 \rightarrow \begin{cases} Z_N, & r \rightarrow 0 \\ 1, & r \rightarrow \infty \end{cases} \tag{9}$$

where $\sum z_j = Z_N - 1$ ($Z_N$ here stands for the nuclear charge). The parameters $\alpha_j$ and $\beta_j$ are optimized to reproduce the HF values accurately.

# 3. Collisional processes in atoms

The most significant advantage of the pseudopotential method is its simplicity. However, it is worth determining the validity of this approach when used for computing collisional processes. In this section, we perform a thorough examination of the pseudopotentials for hydrogen and lithium by comparing the cross sections of four inelastic processes: proton-impact excitation, proton-impact ionization, charge exchange, and photoionization. The initial and final states of the targets are obtained by solving the corresponding Schrödinger equation. For the hydrogen atom, we compare the pseudopotential results with the exact analytical solutions. Furthermore, in order to assess the applicability of the depurated inversion method, we compute the photoionization of more complex many-electron atoms and compare our findings with experimental data.

## 3.1 Proton-impact excitation

The proton-impact excitation of target $X$ is defined as

$$\mathrm{H}^+ + X \rightarrow \mathrm{H}^+ + X^*. \tag{10}$$

The excitation cross section $\sigma$ of the target from the initial bound state $\psi_i$ to the excited state $\psi_f$ may be written as

$$\sigma = \frac{\mu^2}{4\pi^2}\frac{k_f}{k_i}\int \left|T_{fi}\right|^2 d\Omega, \tag{11}$$

where $\mu$ is the reduced mass of the proton–atom system, $\mathbf{k}_i$ and $\mathbf{k}_f$ are the initial and final relative momenta, and

$$T_{fi} = \langle \psi_f | V | \psi_i \rangle \tag{12}$$

is the transition-matrix or T-matrix. If the initial and final states of the transition are described by the Hartree–Fock method, the orbitals will give the correct high energy limit in the first-order approximation (this is not the case for the charge exchange process). Hence, we will concentrate our computing efforts in the first perturbative order of the transition-matrix element through the FBA, given by

$$T_{fi}^{\mathrm{FBA}} = \tilde{V}(\mathbf{p}) F_{fi}(\mathbf{p}). \tag{13}$$

The term $F_{fi}(\mathbf{p})$ is the form factor

$$F_{fi}(\mathbf{p}) = \frac{1}{(2\pi)^{3/2}} \int \tilde{\psi}_f^*(\mathbf{k})\tilde{\psi}_i(\mathbf{k}+\mathbf{p})\, d\mathbf{k}, \tag{14}$$

where $\mathbf{p}$ is the momentum transfer vector

$$\mathbf{p} = p_{\min}\hat{\mathbf{v}} + \boldsymbol{\eta}, \tag{15}$$

$$p_{\min} = \frac{\varepsilon_f - \varepsilon_i}{v} \to \begin{cases} \infty, & v \to 0 \\ 0, & v \to \infty \end{cases}, \tag{16}$$

$\hat{\mathbf{v}}$ is the ion velocity, $\boldsymbol{\eta}$ is the transversal momentum transfer, so that $\hat{\mathbf{v}} \cdot \boldsymbol{\eta} = 0$, whereas $\varepsilon_i$ and $\varepsilon_f$ are the binding energies corresponding to the initial and final states. A more comprehensive formulation of the FBA can be found, for instance, in Ref. 21.

The first Born proton-impact excitation cross sections of hydrogen and lithium from the ground states are shown in Fig. 5. The pseudopotential results for the $f_1 = 2s$, $2p$ and $f_2 = 3s$, $3p$, $3d$ final states of hydrogen agree excellently with the analytical expression. For lithium, the pseudopotential cross sections agree in a broad velocity range with the DIM calculations, except for low proton-impact velocities. This disagreement arises from the form factor. For low impact velocities, the momentum transfer vector is large (16). As discussed earlier, in this region the bound momentum orbital $\tilde{\psi}(\mathbf{k}+\mathbf{p})$ is not described adequately by the pseudopotentials. An alternative expression for the form factor can be considered by implementing the peaking approximation

$$F_{fi}(\mathbf{p}) \sim \tilde{\psi}_i(\mathbf{p})\tilde{\psi}_f^*(0) + \tilde{\psi}_f(\mathbf{p})\tilde{\psi}_i^*(0). \tag{17}$$

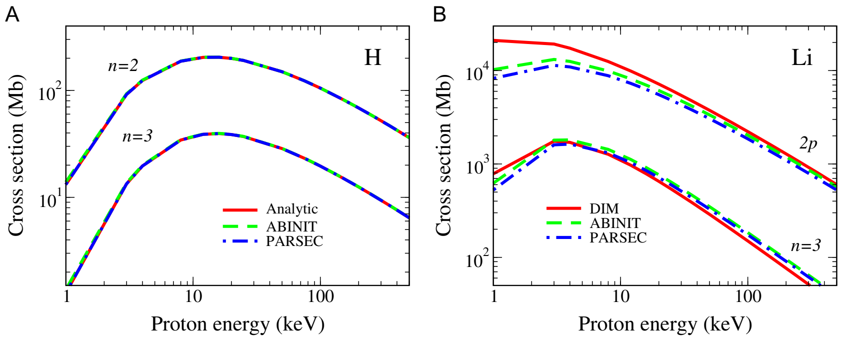

**Fig. 5** Proton-impact excitation cross section from the ground state for (A) hydrogen and (B) lithium.

Therefore, in order to have the correct form factor, it is necessary to obtain an accurate description of the initial bound state at large momentum values, which is not the case for the pseudostates (see Fig. 3B) and hence their failure when used in the cross section calculation.

## 3.2 Proton-impact ionization

The transition matrix (12) for the proton-impact ionization of $X$,

$$\mathrm{H}^+ + X \rightarrow \mathrm{H}^+ + X^+ + e^-, \tag{18}$$

can also be written in terms of the first-order Born approximation. In this case, the final state $\psi_f$ in Eq. (14) is an outgoing continuum wavefunction $\psi_{\mathbf{k}_f}^-$, while $\varepsilon_f = k_f^2/2$ is the energy of the ionized electron.

The single-differential proton-impact ionization cross sections $d\sigma/d\varepsilon_f$ of hydrogen and lithium at a proton velocity of $v_p = 1$ a.u. are shown in Fig. 6. In the case of hydrogen, the pseudopotential and analytical results agree for all the electron energy range, except at very high values. On the other hand, for lithium, the cross sections computed with pseudopotentials only agree at low energies. Once again, assuming that $\psi_{\mathbf{k}_f}^-(\mathbf{k})$ can be approximated by a plane wave, the form factor is reduced to the Fourier transform of the initial bound state

$$F_{fi}(\mathbf{p}) \sim \tilde{\psi}_i(\mathbf{p} - \mathbf{k}_f). \tag{19}$$

Then, as $k_f$ increases, so does $p_{\min}$, and the form factor is not well represented by the pseudopotentials. The significant discrepancies shown in Fig. 6 provide another demonstration of how a wrong description of the momentum space wavefunction may produce huge errors in collisional processes calculations.

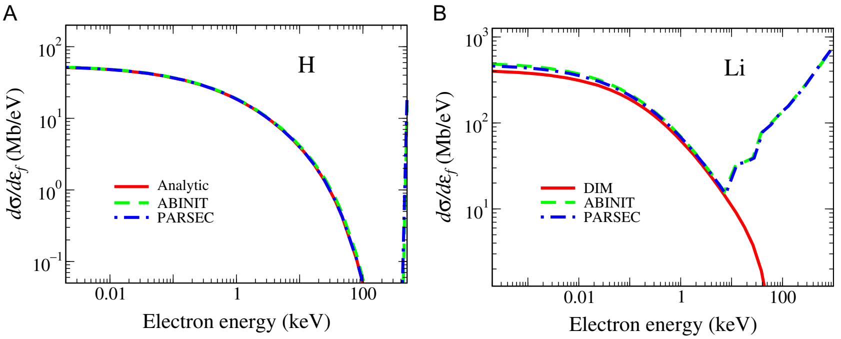

**Fig. 6** Single differential proton-impact ionization cross section from the ground state of (A) hydrogen and (B) lithium at $v_p = 1$ a.u.

## 3.3 Proton-impact charge exchange

The proton-impact charge exchange of target $X$ is defined as

$$\mathrm{H}^+ + X \rightarrow \mathrm{H} + X^+. \tag{20}$$

The charge transfer cross section by the collision of a proton (electron capture) is computed with the first-order Brinkman–Kramers approximation.[22] Accordingly, the matrix element is defined by

$$T_{fi}^{\mathrm{BK}} = \tilde{\psi}_f^*(\mathbf{W}_f)\left[\varepsilon_f - \frac{W_f^2}{2}\right]\tilde{\psi}_i(\mathbf{W}_i), \tag{21}$$

where $\mathbf{W}_i$ and $\mathbf{W}_f$ are the momentum transfer vectors

$$\mathbf{W}_i = W_{i0}\hat{\mathbf{v}} + \boldsymbol{\eta}, \quad W_{i0} = \frac{v}{2} - p_{\min} \tag{22}$$

$$\mathbf{W}_f = W_{f0}\hat{\mathbf{v}} + \boldsymbol{\eta}, \quad W_{f0} = \frac{v}{2} + p_{\min}, \tag{23}$$

and they satisfy the condition $\mathbf{W}_i + \mathbf{W}_f = \mathbf{v}$, and $p_{\min}$ is defined in Eq. (16).

The charge exchange cross sections of hydrogen and lithium in the ground state are illustrated in Fig. 7. The cross section of hydrogen is described with high accuracy by the pseudopotential approach for a wide range of proton velocities. However, this process constitutes a symmetrical resonance, i.e., $\varepsilon_f = \varepsilon_i$, and the agreement may be misleading. For the lithium case, the pseudopotentials fail utterly to describe the electron capture correctly at low and high velocities. For low and high $v_p$ values, the momentum transfer vector becomes large, and therefore, the cross sections calculated with pseudopotentials disagree completely for most of the energy values.

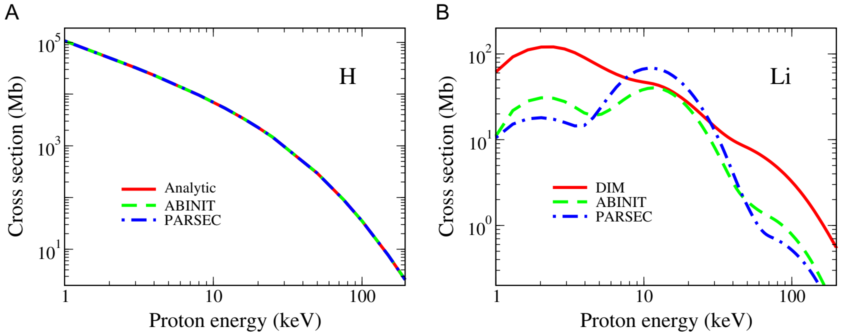

**Fig. 7** Proton-impact electron capture cross section for (A) hydrogen and (B) lithium in the ground state.

## 3.4 Photoionization

The single photoionization is defined as

$$\hbar\omega + X \rightarrow X^{+} + e. \tag{24}$$

Considering a perturbative photon field, the initial bound $\psi_i$ and final continuum $\psi^{-}_{\mathbf{k}_f}$ states of the target are not significantly distorted; therefore, the relevant matrix element of the photoionization process is given by

$$T^{\mathrm{Ph}}_{\mathbf{k}} = \int \psi^{-}_{\mathbf{k}_f}(\mathbf{r})[-i\hat{\varepsilon}_{\lambda} \cdot \nabla_{\mathbf{r}}]\psi_i(\mathbf{r}), \tag{25}$$

where $\hat{\varepsilon}_{\lambda}$ is the polarization versor and $\mathbf{k}_f = \sqrt{2(\omega + \varepsilon_i)}$, as imposed by energy conservation.

The first-order photoionization cross sections of hydrogen and lithium are shown in Fig. 8. The pseudopotentials results for the hydrogen atom agree with the exact analytical expression results only for low photon energies, failing at larger values. These discrepancies can be understood considering the continuum wavefunction $\psi^{-}_{\mathbf{k}_f}(\mathbf{r})$ as a plane wave. Consequently, the matrix element $T^{\mathrm{Ph}}_{\mathbf{k}}$ is reduced to

$$T^{\mathrm{Ph}}_{\mathbf{k}} \sim -\left(\hat{\varepsilon}_{\lambda} \cdot \mathbf{k}_f\right)\tilde{\psi}_i\left(\mathbf{k}_f\right), \tag{26}$$

and it is determined entirely by the behavior of the bound target pseudostate in the momentum representation. For hydrogen, the pseudo-orbital from PARSEC in the Fourier space coincides with the exact analytical solution for the entire range of $k$, which explains the excellent agreement in the cross section results. For lithium, the pseudopotential cross sections disagree with

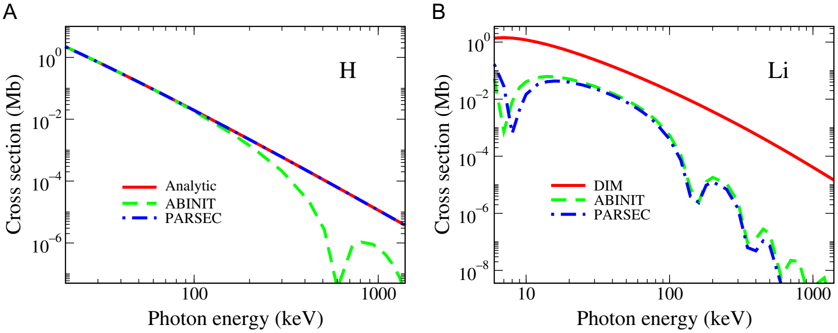

**Fig. 8** Single photoionization cross section for (A) hydrogen and (B) lithium.

the DIM results for all energy values. The large oscillations in the cross sections are originated by the spurious oscillatory structure of the bound state for large $k$ values (see inset of Fig. 3B).

### 3.5 DIM Photoionization of many-electron atoms

In order to assess the applicability of the depurated inversion method for atoms with a more complex structure, we compute the photoionization of many-electron targets with the DIM potentials[4] and compare our results with experimental values. The first-order photoionization cross section of nitrogen and neon are shown in Fig. 9. Experimental data from[23–26] is illustrated with hollow symbols. The DIM photoionization cross sections of these atoms agree excellently with the experimental values for low, medium and high photon energies. For neon, discrepancies start to be noticeable for low and intermediate energy. An accurate photoionization description of heavier atoms requires the inclusion of many-body effects that can be relevant, such as orbital relaxation due to the creation of a hole, collective response of inner shell electrons[27] and correlation effects.

## 4. Depurated inversion method for molecules

The depurated inversion method described above is extended here to determine effective potentials for molecules; methane is taken as an example. Furthermore, the molecular description of $CH_4$ given by DIM is tested by computing two collisional processes within the FBA.

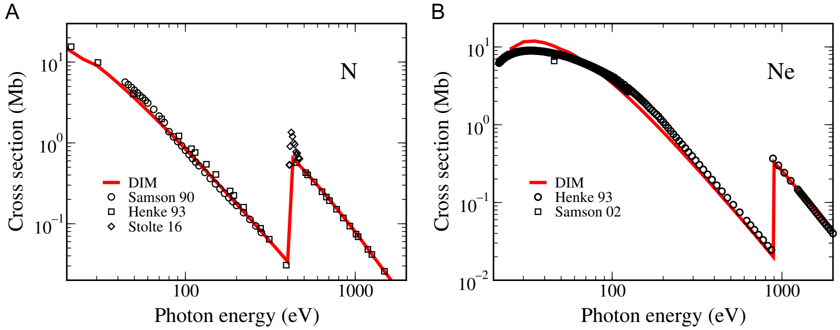

**Fig. 9** Single photoionization cross section for (A) nitrogen and (B) neon.

## 4.1 Theory

Without loss of generality, we will present the DIM theoretical grounds for hydride compounds. The Hamiltonian of an $N$-electron $X\,H_n$ molecule within the Born–Oppenheimer approximation is given by

$$\mathcal{H} = -\sum_{i=1}^{N} \frac{1}{2}\nabla_{\mathbf{r}_i}^2 - \sum_{i=1}^{N} \frac{Z_N}{r_i} + \sum_{i=1}^{N} V_H(r_i) + \sum_{i<j}^{N} \frac{1}{r_{ij}}, \tag{27}$$

$$V_H(r_i) = -\sum_{j=1}^{n} \frac{1}{\left|\mathbf{r}_i - \mathbf{R}_{H_j}\right|}, \tag{28}$$

where $Z_N$ is the nuclear charge of the heavier atom, and $\mathbf{R}_{H_j}$ are the coordinates of the hydrogens respect to the $X$ atom. The corresponding Schrödinger equation $\mathcal{H}\Psi = E\Psi$ is solved and the orbitals are expressed as in Eq. (5) considering the single-center expansion (SCE). The orbitals and energies are found by solving the Hartree–Fock equations. The computation of these equations generally relies on the use of finite basis sets for the representation of the molecular orbitals (MOs). Usually, the MOs are expressed as a linear combination of atomic orbitals (LCAO),

$$\Psi_i = \sum_j c_{ji}\phi_j, \tag{29}$$

which can be constructed with Gaussian-type orbitals (GTO) basis sets.

The inverted molecular potential expression, analogous to Eq. (8), obtained from GTO basis sets present more difficulties than the atomic case. In addition to the asymptotic divergences and the poles, large unphysical oscillations arise.[28–31] These prominent oscillations originate from undulations present in the MOs due to the finite number of the basis set. The second derivative, necessary to evaluate the inversion formula, amplifies these features.[28,31] In some cases, the oscillations are huge, e.g., near an electronegative atom like Cl. The appearance of these oscillations in the inverted potentials forces us to incorporate further actions in the depuration scheme. To illustrate this procedure, we consider the 1$s$ orbital of the carbon atom. We solved the Hartree–Fock equations using the 6-311G basis set with GAMESS code[32,33] and obtained inverted potentials by implementing Eq. (8). The resulting $Z_{1s}^{6-311\mathrm{G}}$ charge is shown in Fig. 10A with a dot-dashed line. The charge oscillates significantly at low distances and diverges for higher $r$ values. The same calculation was repeated using the universal Gaussian basis set (UGBS), which has a more significant amount of primitives. The corresponding inverted charge $Z_{1s}^{\mathrm{UGBS}}$ is exhibited in the figure

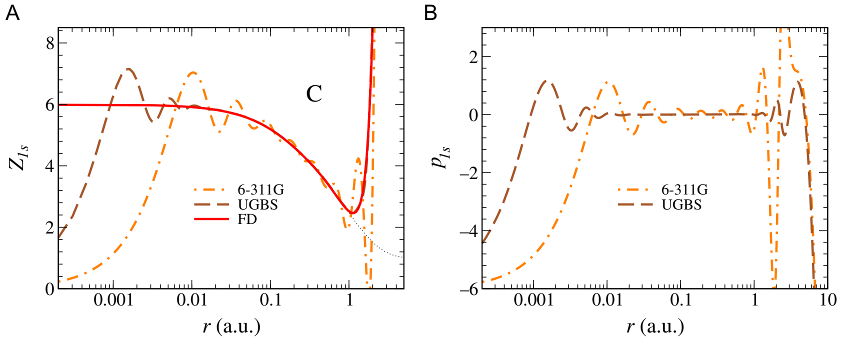

**Fig. 10** (A) Effective charges for the 1*s* orbital of carbon. (B) Basis-set oscillation profiles.

with a dashed line. Although the charge still diverges around $r \approx 1$a.u., the oscillations are now circumscribed near the nucleus. Finally, the differential Hartree–Fock equations for the carbon atom were solved using the finite-differences (FD) method. The 1*s* inverted charge obtained with this procedure, $Z_{nl}^{\mathrm{FD}}$ (solid line) shows no oscillations since no basis sets have been used to construct the orbital; however, the charge still diverges for $r > 1$a.u., as it usually does for all HF calculations.

The oscillations pattern will vary for each basis set used in the calculations. We may define oscillation profiles as

$$p_{nl}^{\mathrm{BS}} = Z_{nl}^{\mathrm{BS}} - Z_{nl}^{\mathrm{FD}}, \tag{30}$$

where $Z_{nl}^{\mathrm{BS}}$ is the inverted charge of the atom using a particular basis set "BS" and $Z_{nl}^{\mathrm{FD}}$ is the effective charge obtained from the inversion of the finite-difference wavefunctions. In the previous example, the basis set considered for calculating the 1*s* orbital of carbon were 6-311G and UGBS. The oscillation profiles for the 1*s* orbital, using Eq. (30) for these basis sets, are shown in Fig. 10B. Since the orbital profiles for each atomic basis set are distinctive, once they are determined for the atomic case, they can be removed in further molecular calculations. An example of this procedure is given in the following section.

## 4.2 Example: Methane

In order to illustrate the implementation of the DIM for molecules, we considered $CH_4$, which is highly symmetric, and therefore, can be described with an angular averaged potential.[34] We computed the HF molecular orbitals and energies of $CH_4$ employing the UGBS basis sets of carbon and hydrogen, which considers angular momenta up to $L = 1$. Methane calculations with this basis set should include polarization functions

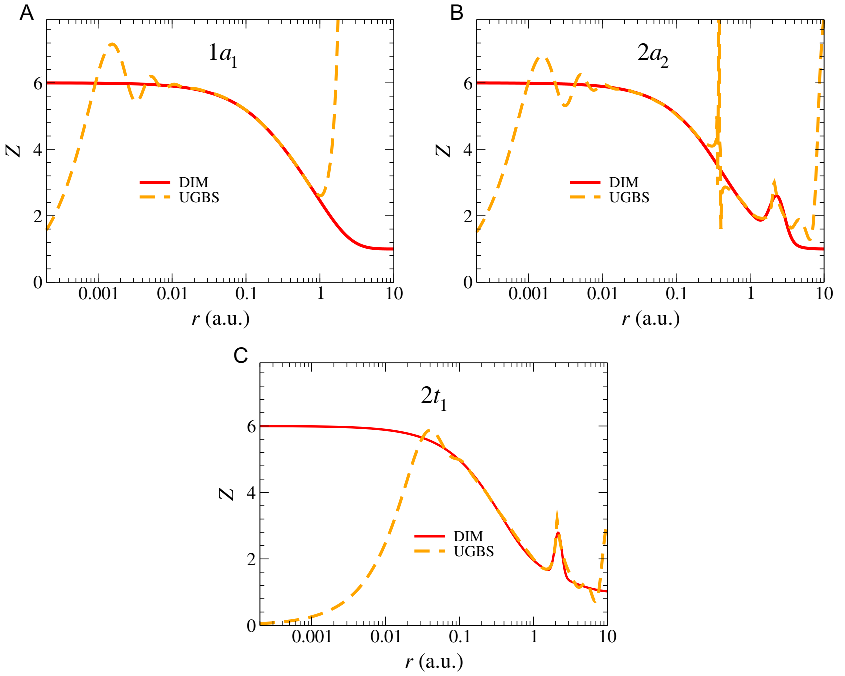

**Fig. 11** (A) $1a_1$, (B) $2a_2$, and (C) $2t_1$ effective charges of $CH_4$; direct inversion (*dashed line*) and depurated inverted (*solid line*).

(at least d-functions) to increase the accuracy of the molecular energies.[35,36] However, to isolate the effects of the basis set, we computed the atomic oscillation profiles and the molecular orbitals on the same footing. The charges obtained by direct inversion are given in Fig. 11 with dashed lines. Since the molecular orbitals are given by LCAO of carbon and hydrogen, the oscillations of the inverted charges are a consequence of the finite basis set of these atoms. To remove the most critical oscillations, first, we must determine the oscillation profiles produced by the atomic carbon basis set. We use Eq. (30) to determine the $p_{1s}^{\mathrm{UGBS}}$, $p_{2s}^{\mathrm{UGBS}}$, and $p_{2p}^{\mathrm{UGBS}}$ profiles of carbon. Then, we remove the oscillations by subtracting the carbon $p_{nl}^{\mathrm{UGBS}}$ profiles from the corresponding inverted charges $Z_i^{\mathrm{UGBS}}$ of $CH_4$. The oscillations are removed for all orbitals except for the $2a_2$, which presents small oscillatory residues from the hydrogen basis set. Since the residual fluctuations are minimum and near the nucleus, we proceeded to implement the depuration scheme as described in Section 2.2. We define a new parametric DIM charge equation,

$$Z(r) = \sum_j Z_j e^{-\alpha_j r} + Z_{\mathrm{H}} e^{-(\ln r - \ln\beta)^2/(2\gamma)} + 1. \tag{31}$$

**Table 1** Energies and fitting parameters for the DIM effective charges (Eq. (31)), for $CH_4$.

| $nl$ | $E$ | $Z$ | $\alpha$ | $\beta$ | $\gamma$ |
|---|---|---|---|---|---|
| $1a_1$ | −11.1949 | 1.925280 | 0.641982 | | |
| | | 0.953120 | 5.571510 | | |
| | | 2.121600 | 1.500440 | | |
| $2a_2$ | −0.9204 | 2.912200 | 3.149990 | | |
| | | 2.087800 | 0.771371 | | |
| | | 1.23640 | | 2.329570 | 0.053420 |
| $2t_1$ | −0.5042 | 0.901953 | 2.895140 | | |
| | | 1.112030 | 0.388649 | | |
| | | 2.986017 | 2.931210 | | |
| | | 1.30182 | | 2.169850 | 0.012616 |

In contrast to the approximation proposed for atoms (9), a second term has been added to the formula to account for the presence of the hydrogens. This expression allows us to conveniently adjust both the location and width of the screened hydrogenic potential without affecting the correct charge value at the origin. The optimized parameters for the methane molecule are given in Table 1, and the corresponding DIM charges are shown in Fig. 11, with solid lines. The orbital energies obtained with these charges are also given in the table.

## 4.3 Collisional processes

The orientation of the molecular targets is important for determining the cross sections of collisional processes. However, it is generally not pre-established in the experiments. Thus, the spherically averaged description of the system assumed by the DIM potential makes sense. In the following, we examine two collisional processes in the first-order approximation: proton-impact ionization and single photoionization.

### *Proton-impact ionization*

Results for the proton-impact ionization cross section for $CH_4$, calculated under the first Born approximation, are given in Fig. 12. The initial bound and the final continuum states of the molecule needed for the T-matrix computation (Eq. (12)) were calculated with the DIM potentials from

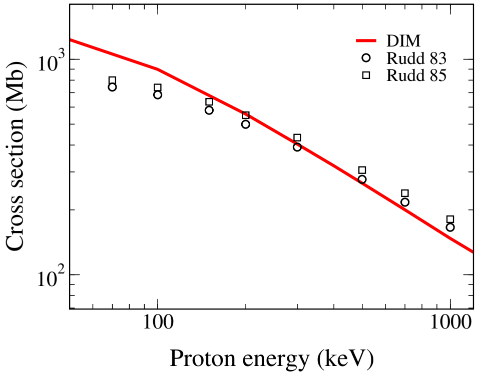

**Fig. 12** Proton-impact ionization cross section for $CH_4$. *Solid line*: first-order DIM theoretical calculations. *Symbols*: experiments from Refs. 37 and 38.

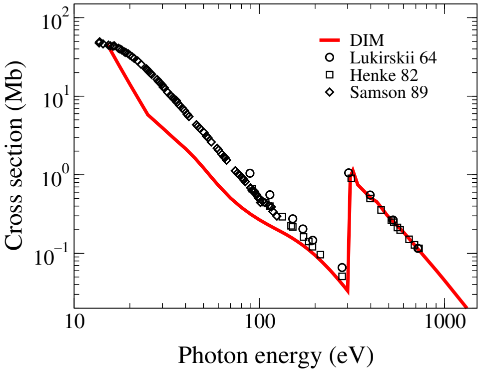

**Fig. 13** Single photoionization cross section of $CH_4$. *Solid line*: first-order DIM theoretical calculations. *Symbols*: experiments from Refs. 39–41.

Section 4.2. The ionization cross section for high and intermediate energies shows good agreement with the experimental results. The failure at low energies is ascribed to the validity of the first Born approximation and not to our DIM approach.

### *Photoionization*

The photoionization cross section for $CH_4$, calculated with the DIM potentials in a first-order approximation, is shown in Fig. 13 (solid lines). Good agreement with the experimental results (symbols) is found for high energy values and at the threshold. The curve between ~15 and ~300 eV shows the photoionization from the outer $n = 2$ shell, while the discontinuity at 300 eV corresponds to the threshold of the $1a_1$ inner shell orbital. For low and intermediate photon energies, the agreement between our calculations and the experimental values from Refs. 39–41 is not that good. Phenomena such as molecular orbital relaxation, possible collective contributions, and correlation effects must be considered in further calculations. On the other hand, for the $1a_1$ inner shell photoionization, these effects are not significant, and we obtain a perfect agreement with the experimental results.

## 5. Concluding remarks

In this work, we explored the possibility of using pseudopotentials within the single electron model to calculate inelastic transitions. The first Born approximation was used to calculate proton-impact excitation, ionization, electron capture, and photoionization. Two simple atoms were studied, having a single electron in the outer shell. For hydrogen, we found excellent agreement for all the collisional processes, for low and intermediate energies. In the case of lithium, the only process that can be calculated with reasonable accuracy is the proton-impact excitation. We concluded that the range of validity is restrained to minimal momentum transfers. The depurated inversion method, on the other hand, accurately reproduces photoionization experimental results for many-electron atoms.

We extended the DIM for molecular systems. In this case, the inversion procedure produces huge oscillations due to the finite size of the basis sets involved in the Hartree–Fock orbital calculations. An additional step is included during the depuration scheme. In order to determine the oscillation profile for a particular basis set, we computed the inverted atomic charges in a finite-differences framework. By subtracting the charges, it is possible to isolate the oscillations corresponding to this particular basis set. We used the DIM method to determine the effective potentials for $CH_4$. These potentials are implemented in first-order proton-impact ionization and photoionization cross sections calculations. For both processes, we found good agreement with the experimental results. The main discrepancies can be attributed to the fact that only first-order is considered in the perturbation theory.

## Acknowledgments

The authors thank the Consejo Nacional de Investigaciones Científicas y Técnicas (CONICET), Universidad de Buenos Aires (UBA) and Agencia Nacional de Promoción Científica y Tecnológica (ANPCyT) for the grants that supported this work.

## References

1. PARSEC Home Page. https://parsec.ices.utexas.edu/styled-2/ (Accessed Jan 18, 2019).
2. Chelikowsky, J. R.; Troullier, N.; Saad, Y. Finite-Difference-Pseudopotential Method: Electronic Structure Calculations Without a Basis. *Phys. Rev. Lett.* **1994**, *72*(8), 1240–1243. https://doi.org/10.1103/PhysRevLett.72.1240.
3. Mendez, A. M. P. *Método de Inversión Depurada para Potenciales Locales en Átomos y Moléculas*. 2015. Tesis de Licenciatura, Universidad Nacional de Salta.
4. Mendez, A. M. P.; Mitnik, D. M.; Miraglia, J. E. Depurated Inversion Method for Orbital-Specific Exchange Potentials. *Int. J. Quantum Chem.* **2016**, *116*(24), 1882–1890. https://doi.org/10.1002/qua.25295.
5. Mendez, A. M. P.; Mitnik, D. M.; Miraglia, J. E. Local Effective Hartree-Fock Potentials Obtained by the Depurated Inversion Method. In *Nov. Electron. Struct. Theory Gen. Innov. Strongly Correl. Syst.*; Hoggan, P. E. Ed.; Advances in Quantum Chemistry.; Vol. 76, Academic Press, 2018; pp 117–132. https://doi.org/10.1016/bs.aiq.2017.07.004.
6. Bates, D. R. Theoretical Treatment of Collisions Between Atomic Systems. *Pure Appl. Phys. Elsevier* **1962**, *13*, 549–621. In At. Mol. Process.; Bates, D. R. Ed.
7. McDowell, M. R. C.; Peach, G. Ionization of Lithium by Fast Protons and Electrons. *Phys. Rev.* **1961**, *121*, 1383–1387.
8. Pindzola, M. S.; Robicheaux, F.; Loch, S. D.; Berengut, J. C.; Topcu, T.; Colgan, J.; Foster, M.; Griffin, D. C.; Ballance, C. P.; Schultz, D. R.; Minami, T.; Badnell, N. R.; Witthoeft, M. C.; Plante, D. R.; Mitnik, D. M.; Ludlow, J. A.; Kleiman, U. The Time-Dependent Close-Coupling Method for Atomic and Molecular Collision Processes. *J. Phys. B* **2007**, *40*, R39–R60.
9. Burke, P. G. *R-Matrix Theory of Atomic Collisions*; Springer-Verlag: Berlin, Heidelberg, 2011.
10. Bray, I.; Abdurakhmanov, I. B.; Bailey, J. J.; Bray, A. W.; Fursa, D. V.; Kadyrov, A. S.; Rawlins, C. M.; Savage, J. S.; Stelbovics, A. T.; Zammit, M. C. Convergent Close-Coupling Approach to Light and Heavy Projectile Scattering on Atomic and Molecular Hydrogen. *J. Phy. B* **2017**, *50*, 202001.
11. Pindzola, M. S.; Colgan, J.; Robicheaux, F.; Lee, T. G.; Ciappina, M. F.; Foster, M.; Ludlow, J. A.; Abdel-Naby, S. A. Time-Dependent Close-Coupling Calculations for Ion-Impact Ionization of Atoms and Molecules. *Adv. At. Mol. Opt. Phys.* **2016**, *65*, 291–319.
12. Kirchner, T.; Gulyás, L.; Lüdde, H. J.; Engel, E.; Dreizler, R. M. Influence of Electronic Exchange on Single and Multiple Processes in Collisions Between Bare Ions and Noble-Gas Atoms. *Phys. Rev. A* **1998**, *58*, 2063–2076.
13. Fiori, M. R.; Jalbert, G.; Bielschowsky, C. E.; Cravero, W. Ionization of Lithium by Impact of Fast Ions. *Phys. Rev. A* **2001**, *64*, 012705.
14. Szabo, A.; Ostlund, N. S. *Modern Quantum Chemistry: Introduction to Advanced Electronic Structure Theory*; Dover Publications, Inc.: Mineola, NY, 1996.
15. Helgaker, T.; JØRgensen, P.; Olsen, J. *Molecular Electronic-Structure Theory*. John Wiley & Sons, Ltd: Chichester, UK, 2000.
16. Schaefer, H. F. *Quantum Chemistry: The Development of Ab Initio Methods in Molecular Electronic Structure Theory*; Dover Publications, Inc: Mineola, NY, 2004.
17. ABINIT Home Page. https://www.abinit.org/psp-tables (Accessed Jan 18, 2019).
18. Hamann, D. R.; Schlüter, M.; Chiang, C. Norm-Conserving Pseudopotentials. *Phys. Rev. Lett.* **1979**, *43*(20), 1494–1497. https://doi.org/10.1103/PhysRevLett.43.1494.
19. Froese Fischer, C.; Brage, T.; Jönsson, P. *Computational Atomic Structure: An MCHF Approach*. Institute of Physics Publishing: Bristol, UK, 1997;p 279.
20. Johnson, W. R. *Atomic Structure Theory : Lectures on Atomic Physics*. Springer: Berlin, Heidelberg, 2007;p 312.

21. McDowell, M. R. C.; Coleman, J. P. *Introduction to the Theory of Ion-Atom Collisions*; North-Holland Publishing Company: Amsterdam, 1970.
22. *C, B. H.*. Kramers, H. A. *Physics.-Zur Theorie der Einfangung von Elektronen durch u.˜Teilchen. Proc. K. Akad. van Wet.* **1930**, *33*, 973–984. http://www.dwc.knaw.nl/DL/publications/PU00015982.pdf.
23. Henke, B. L.; Gullikson, E. M.; Davis, J. C. X-Ray Interactions: Photoabsorption, Scattering, Transmission, and Reflection at E = 50-30,000 eV, Z = 1-92. *At. Data Nucl. Data Tables* **1993**, *54*(2), 181–342. https://doi.org/10.1006/ADND.1993.1013.
24. Samson, J. A. R.; Angel, G. C. *Single- and double-photoionization cross sections of atomic nitrogen from threshold to 31 Å. Phys. Rev. A* **1990**, *42*(3), 1307–1312. https://doi.org/10.1103/PhysRevA.42.1307. https://link.aps.org/doi/10.1103/PhysRevA.42.1307.
25. Samson, J. A. R.; Stolte, W. C. Precision Measurements of the Total Photoionization Cross-Sections of He, Ne, Ar, Kr, and Xe. *J. Electron Spectros. Relat. Phenomena* **2002**, *123*(2–3), 265–276. https://doi.org/10.1016/S0368-2048(02)00026-9.
26. Stolte, W. C.; Jonauskas, V.; Lindle, D. W.; Sant'Anna, M. M.; Savin, D. W. *Inner-Shell Photoionization Studies of Neutral Atomic Nitrogen. Astrophys. J.* **2016**, *818*(2), 149. https://doi.org/10.3847/0004-637X/818/2/149. http://stacks.iop.org/0004-637X/818/i=2/a=149?key=crossref.2b86a13e417a21fe226f2d7fdc09b8c8.
27. Ederer, D. L. Photoionization of the 4d Electrons in Xenon. *Phys. Rev. Lett.* **1964**, *13*(25), 760–762. https://doi.org/10.1103/PhysRevLett.13.760.
28. Schipper, P. R. T.; Gritsenko, O. V.; Baerends, E. J. Kohn-Sham potentials corresponding to Slater and Gaussian basis set densities. *Theor. Chem. Accounts Theory, Comput. Model. (Theoretica Chim. Acta)* **1997**, *98*(1), 16–24. https://doi.org/10.1007/s002140050273.
29. Mura, M. E.; Knowles, P. J.; Reynolds, C. A. Accurate Numerical Determination of Kohn-Sham Potentials From Electronic Densities: I. Two-Electron Systems. *J. Chem. Phys.* **1997**, *106*(23), 9659–9667. https://doi.org/10.1063/1.473838.
30. Jacob, C. R. Unambiguous Optimization of Effective Potentials in Finite Basis Sets. *J. Chem. Phys.* **2011**, *135*(24), 244102. https://doi.org/10.1063/1.3670414.
31. Gaiduk, A. P.; Ryabinkin, I. G.; Staroverov, V. N. *Removal of Basis-Set Artifacts in KohnSham Potentials Recovered From Electron Densities. J. Chem. Theory Comput.* **2013**, *9*(9), 3959–3964. https://doi.org/10.1021/ct4004146. http://www.ncbi.nlm.nih.gov/pubmed/26592391.
32. Schmidt, M. W.; Baldridge, K. K.; Boatz, J. A.; Elbert, S. T.; Gordon, M. S.; Jensen, J. H.; Koseki, S.; Matsunaga, N.; Nguyen, K. A.; Su, S.; Windus, T. L.; Dupuis, M.; Montgomery, J. A. General Atomic and Molecular Electronic Structure System. *J. Comput. Chem.* **1993**, *14*(11), 1347–1363. https://doi.org/10.1002/jcc.540141112.
33. Gordon, M. S.; Schmidt, M. W. Advances in Electronic Structure Theory: GAMESS a Decade Later. In *Theory Appl. Comput. Chem.*; Dykstra, C. E., Frenking, G., Kim, K. S., Scuseria, G. E., Eds.; Elsevier: Amsterdam, 2005; pp 1167–1189. chap. 41. https://doi.org/10.1016/B978-044451719-7/50084-6.
34. Granados-Castro, C. M. Application of Generalized Sturmian Basis Functions to Molecular Systems. Ph.D. thesis, Université de Lorraine, Metz, France and Universidad Nacional del Sur, Bahía Blanca, Argentina 2016.
35. Rothenberg, S.; Schaefer, H. F. Methane as a Numerical Experiment for Polarization Basis Function Selection. *J. Chem. Phys.* **1971**, *54*, 2764–2766.
36. Hariharan, P. C.; Pople, J. A. The Effect of D-Functions on Molecular Orbital Energies for Hydrocarbons. *Chem. Phys. Lett.* **1972**, *16*, 217–219.

37. Rudd, M. E.; DuBois, R. D.; Toburen, L. H.; Ratcliffe, C. A.; Goffe, T. V. Cross Sections for Ionization of Gases by 5-4000-keV Protons and for Electron Capture by 5-150-keV Protons. *Phys. Rev. A* **1983**, *28*(6), 3244–3257. https://doi.org/10.1103/PhysRevA.28.3244.
38. Rudd, M. E.; Kim, Y. K.; Madison, D. H.; Gallagher, J. W. Electron Production in Proton Collisions: Total Cross Sections. *Rev. Mod. Phys.* **1985**, *57*(4), 965–994. https://doi.org/10.1103/RevModPhys.57.965.
39. Lukirskii, A. P.; Brytov, I. A.; Zimkina, T. M. *Optika I Spektr.* Vol. 17, 1964234. www.scopus.com.
40. Henke, B. L.; Lee, P.; Tanaka, T. J.; Shimabukuro, R. L.; Fujikawa, B. K. Low-energy X-ray Interaction Coefficients: Photoabsorption, Scattering, and Reflection: E = 1002000 eV Z = 194. *At. Data Nucl. Data Tables* **1982**, *27*(1), 1–144. https://doi.org/10.1016/0092-640X(82)90002-X.
41. Samson, J. A. R.; Haddad, G. N.; Masuoka, T.; Pareek, P. N.; Kilcoyne, D. A. L. Ionization Yields, Total Absorption, and Dissociative Photoionization Cross Sections of CH4 from 110 to 950 Å. *J. Chem. Phys.* **1989**, *90*(12), 6925–6932. https://doi.org/10.1063/1.456267.